MSC-00149

NATIONAL AERONAUTICS AND SPACE ADMINISTRATION

NASA PROGRAM APOLLO WORKING PAPER

THERMAL EVALUATION OF THE EARLY APOLLO SCIENTIFIC EXPERIMENT PACKAGE ISOTOPE HEATER MODELS IN THE MSC 1.5-MEGAWATT ARC-HEATED FACILITY

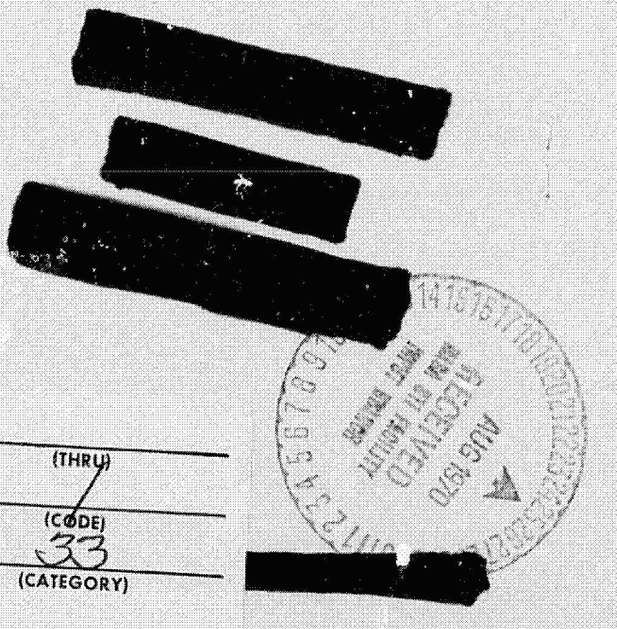

MANNED SPACECRAFT CENTER
HOUSTON, TEXAS

September 8, 1969

MSC-00149

NASA PROGRAM APOLLO WORKING PAPER

THERMAL EVALUATION OF THE EARLY APOLLO SCIENTIFIC EXPERIMENT PACKAGE ISOTOPE HEATER MODELS IN THE MSC 1.5-MEGAWATT ARC-HEATED FACILITY

PREPARED BY

Donald J. Tillian
Thermal Technology Branch

AUTHORIZED FOR DISTRIBUTION

for Maxime A. Faget
Director of Engineering and Development

NATIONAL AERONAUTICS AND SPACE ADMINISTRATION
MANNED SPACECRAFT CENTER
HOUSTON, TEXAS
September 8, 1969

CONTENTS

TABLES

FIGURES

THERMAL EVALUATION OF THE EARLY APOLLO SCIENTIFIC EXPERIMENT PACKAGE ISOTOPE HEATER MODELS IN THE MSC 1.5-MEGAWATT ARC-HEATED FACILITY

By Donald J. Tillian

SUMMARY

Three early Apollo scientific experiment package isotope heater models were tested in the Manned Spacecraft Center 1.5-megawatt arc-heated facility on February 4 and 5, 1969. The test environment simulated the reentry heating conditions on the isotope canisters during a 6.25° lunar-return abort trajectory. The data presented include environmental test conditions, graphite ablation data, model surface temperature response, and photographs of the models before and after testing. These tests demonstrated the structural integrity of the early Apollo scientific experiment package canisters for a nominal lunar abort entry trajectory.

INTRODUCTION

The early Apollo scientific experiment package (EASEP), scheduled for placement on the lunar surface during the first Apollo lunar landing, contains two 15-watt radioisotope heaters for thermal control of the experiment. Joint NASA/Atomic Energy Commission (AEC) safety review and approval of the experiment is required before the flight, since the isotope heaters contain plutonium oxide microspheres. Dispersal and melting of this radioactive material would constitute an inhalation hazard if the graphite canister should fail during an abort earth entry. In view of these considerations, a ground-test program was conducted to support the analytical studies which define probable failure modes and to demonstrate the structural and thermal integrity of the isotope heaters under severe hyperthermal conditions.

Three arc-jet tests of the isotope heater models were conducted in the MSC 1.5-megawatt arc-heated facility. The test conditions, which were representative of a nominal lunar-return abort trajectory, provided an assessment of the thermal-stress conditions affecting the structural

integrity of the isotope heater models. The models were tested at step heating pulse levels of $\dot{q}\sqrt{R}$ of 240 to 533 Btu/ft$^{3/2}$-sec, test gas enthalpy levels from 1^{l}, 000 to 22 200 Btu/lb, and model impact pressures from 0.067 to 0.12 atmosphere. The results of this test program are presented in this report.

SYMBOLS

C_p specific heat of slug material

C_{p_w} specific heat of water

H_t average total enthalpy of gas stream

I arc current

K thermal conductivity

$\dot{m}_g$ gas flow rate

$\dot{m}_w$ water flow rate

$\dot{q}$ incident heat transfer rate

R radius of constantan disk

V arc voltage

ΔT temperature differential between center of periphery of constantan disk

ΔT_w water temperature rise

ρ density

τ thickness

TEST MODELS

The test models, furnished by the Sandia Corporation, were flat-face cylinders 3 inches in diameter and 3 inches in length. Figure 1 shows the test model configuration and the materials of construction in the isotope heater. Temperature-sensitive paints were applied to the titanium canister to evaluate the maximum temperature reached during the arc-jet tests.

A 3/8-16 thread was machined in the graphite model for attachment to sting mounts. Graphite and tantalum stings were used in mounting the test models to the insertion arms. A graphite calibration model (fig. 2) was fabricated to evaluate the heating rate distribution across the model surface during the test.

TEST APPARATUS, CONDITIONS, AND PROCEDURE

Test Apparatus

The 3-inch-diameter test models were exposed to the high enthalpy gas stream produced by the MSC 1.0-megawatt segmented constrictor arc heater. Details of the design and operating characteristics of this arc heater are described in Electro-Optical Systems, Inc., Report 6320, "High Enthalpy Gas Heater," by Robert Richter, dated December 1965. The arc-heated gas stream exits through a 6.0-inch-diameter conical nozzle into a vacuum chamber. Figure 3 shows the arc heater on the vacuum chamber with associated model insertion equipment.

Chamber static pressure was adjusted during each test to provide the desired environmental conditions. The arc-heater operating conditions and test environments are tabulated in table I.

Test Conditions

The predicted cold-wall heating rate and model stagnation pressure histories for the isotope heater during a 6.25° lunar-return abort trajectory are shown in figure 4. Due to the rigid time schedule of the EASEP experiment and the timely need for the arc-jet test results, a true trajectory heating simulation was not attempted. Multiple constant heating pulses were selected to simulate the entry heating environment history. The tests were conducted at a constant gas flow rate, and the arc current was manually adjusted to provide the heating rate conditions shown in figure 5.

The total enthalpy of the arc-heated stream was determined by the energy balance technique. The average total enthalpy of the arc-heated stream was calculated using the following experimental data.

1. Electrical power to the arc heater
2. Gas flow into the arc heater
3. Cooling water flow rates
4. Cooling water inlet and outlet temperatures

The following equation was applied in calculating the average enthalpy of the arc-heated gas stream.

$$H_t = \frac{0.948VI - \dot{m}_w C_{p_w} \Delta T_w}{\dot{m}_g}$$

where C_{p_w} = specific heat of water

H_t = average total enthalpy of gas stream

I = current

$\dot{m}_g$ = gas flow rate

$\dot{m}_w$ = water flow rate

V = voltage

ΔT_w = water temperature rise

Heating rates were measured prior to the model tests using commercial circular foil calorimeters. The sensor output is based on the measurement of a temperature gradient between the center and periphery of a thin constantan disk. This temperature difference is directly

proportional to the heating rate and can be expressed by the following equation.

$$\dot{q} = \frac{4\tau K}{R^2} \Delta T$$

where K = thermal conductivity of constantan

$\dot{q}$ = incident heat transfer rate

R = radius of the constantan disk

ΔT = temperature differential between center and periphery of the constantan disk

τ = thickness of constantan disk

The sensors were calibrated by the manufacturer using a radiant energy source in terms of millivolt output versus the measured incident heating rate.

The heating rate values $q\sqrt{R}$ for the tests were established by measurements from a 1.0-inch-diameter heat transfer rate sensor installed in a 4.0-inch-diameter blunt hemisphere graphite model. Appropriate shape and radius correction factors were used in calculating the effective heat transfer rate $q\sqrt{R}$ for the test models. Heat transfer rate distributions were obtained for the canister model configuration using the graphite calibration model shown in figure 2. The calibration model was instrumented with 1/4-inch-diameter slug calorimeters which measured the relative heating rates at different locations on the model surface. The slug calorimeters contained a known mass of copper which was mounted in a copper body and insulated by an air gap. A chromel-constantan thermocouple was attached to the center of the copper slug. The heat transfer rate measured by this type of calorimeter can be calculated using the equation.

$$\dot{q} = \rho\tau C_p \frac{dT}{dt}$$

where C_p = specific heat of slug material

ρ = density of copper slug

$\dot{q}$ = incident heat transfer rate

τ = thickness of slug

$\frac{dT}{dt}$ = rate of change of temperature of slug with time

The heat transfer rates measured by these calorimeters are presented in table II. The heat transfer rate measurements are considered a reasonable representation of the relative heating rate distribution across the model surface. However, the absolute magnitudes may be in error because of the extremely short test times (less than 1 second) which were necessary to prevent melting of the copper slugs at the high heat transfer rates.

Model impact pressures were measured during calibration tests with a pitot pressure probe. These measurements were taken across the arc-jet stream at the model test conditions and are presented in figures 6 and 7.

The model surface temperatures were measured by a total radiation radiometer which had a lower wavelength limit of 4 microns. The radiometer was mounted on the tunnel door, and mirrors were used to focus on a 1/2-inch-diameter spot on the graphite cylinder. It was not possible to observe the model stagnation point because of the view angle. The surface temperature data obtained at a point approximately 45° off the stagnation line are presented in figure 8.

Test Procedure

The following procedures were used to provide test conditions which simulated the flight trajectory.

After the arc-jet operating conditions for the first heating pulse were established, the heating rate calibration model was inserted into the stream to compare with previous measurements obtained during the calibration tests. After removal of the calibration model, the test model was inserted into the arc-heated stream. If multiple heating rate levels were required, current adjustments were made to provide the necessary test conditions. The arc-jet was turned off at the end of the required test time, and the model remained in the tunnel under vacuum conditions for a period of 15 to 20 minutes. This technique was used to prevent oxidation of the hot graphite surface during the cooldown period.

All of the pertinent data associated with the operation of the arc-jet and vacuum chamber were recorded on magnetic tape with a 50-channel,

analog-to-digital recording system. In addition, the important temperature and pressure data were recorded on strip chart recorders for real-time display. At the completion of testing, the specimens were weighed to determine weight loss, and dimensional measurements were made to determine surface recession. Photographs of the test models were taken before and after testing.

RESULTS AND DISCUSSION

The model ablation data obtained during this test program are summarized in table III. Photographs of the models before and after tests are shown in figures 9 to 26.

Test model FP-3 was tested with a graphite sting at the maximum heating rate and for the total heat load anticipated during the 6.25° lunar-return abort trajectory shown in figure 5. This test condition was selected because it represented the most severe heating environment to which the model could be subjected, and the results would indicate any apparent thermal-stress problems in the model design. The test model survived the severe environment, and post-test inspection did not reveal any cracks or unusual irregularities in the test model surface.

Test model FP-4 was subjected to the three-step heating pulse shown in figure 5. This environment was more representative of the actual heating rate history and total test time of the predicted trajectory. The total test heat load was greater than the predicted flight value to compensate for heat conduction into the model mounting sting during the arc-jet test. The graphite sting failed when the model had been in the arc-heated stream for 131 seconds. The model dropped to a water-cooled region between the model insertion arms. Inspection of the model after the test revealed a fine hairline crack along the surface in the stagnation region. The crack was attributed to the impact or the thermal shock, or both, associated with the contact of the hot graphite surface with the cooled tunnel surface.

To resolve the uncertainity of the origin of the crack, another test model (FP-2) was subjected to the same test conditions for the required total test time of 140 seconds. During this test, a tantalum sting was used in mounting the test model. Post-test inspection of the model did not reveal any cracks or unusual surface phenomena.

The temperature-sensitive paint indicated that the temperature of the titanium canisters exceeded 800° F during each test; however, inspection of the interior components of the models did not indicate any significant thermal degradation effects.

The thermal performance of the isotope heater models was considered satisfactory for both test conditions. The test results demonstrated the structural integrity of the canisters for a nominal lunar abort entry trajectory.

CONCLUDING REMARKS

Three test models of the 15-watt radioisotope heaters used for thermal control of the early Apollo scientific experiment package were tested in the Manned Spacecraft Center 1.5-megawatt arc-heated facility. The test models were subjected to the heating rate and heat load environments associated with entry during a 6.25° lunar abort mission.

Inspection of the models after the tests did not reveal any significant thermal degradation effects. The most significant result from this test program was the demonstration of satisfactory thermal and structural response of the isotope heater canisters for a nominal lunar abort trajectory.

TABLE I.- TEST CONDITIONS FOR EASEP ISOTOPE HEATER MODELS

Test	Model	Condition no.	Test time, sec
453	FP-3	2	57
454	FP-4	1	40
454	FP-4	2	20
454	FP-4	1	71
455	FP-2	1	40
455	FP-2	2	20
455	FP-2	1	82

Condition 1

Arc current, amps.	750
Arc voltage, volts	670
Gas flow rate, lb/sec. . .	0.022
Enthalpy, Btu/lb	14 000
Heat transfer rate, $Btu/ft^{3/2}$-sec	240
Impact pressure, atm . . .	0.067
Test chamber pressure, atm	0.013

Condition 2

Arc current, amps.	1150
Arc voltage, volts	720
Gas flow rate, lb/sec. . .	0.022
Enthalpy, Btu/lb	22 200
Heat transfer rate, $Btu/ft^{3/2}$-sec	533
Impact pressure, atm . . .	0.12
Test chamber pressure, atm	0.013

TABLE II.- HEATING RATE DISTRIBUTION ON A 3-INCH-DIAMETER CYLINDER

Test	Arc current, amps	Arc voltage volts	Gas flow rate, lb/sec	Enthalpy, Btu/lb	Measured heat transfer rates, Btu/ft^2-sec							
					3	7	8	9	10	16	4	9
466	750	670	0.022	14 000	590	590	765	10	9	14	*	>7
467	1150	720	0.022	22 200	*	1080	1305	30	48	61	*	17

Note: * = erratic output.

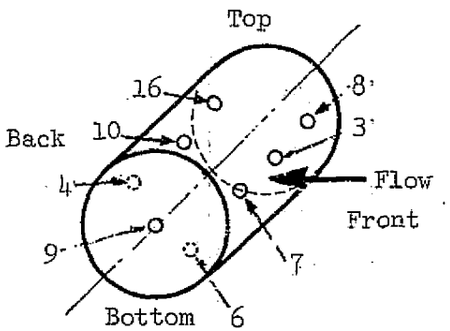

Oblique view

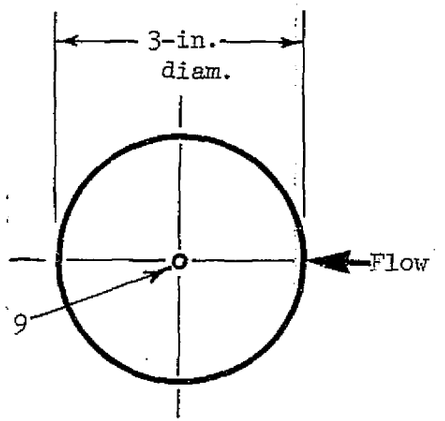

End view

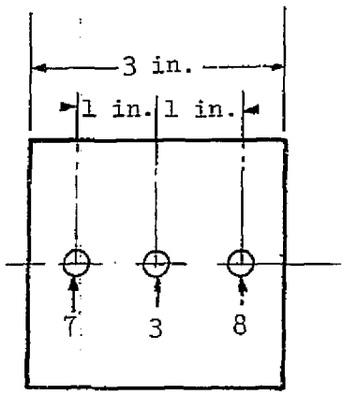

Front (side) view

TABLE III.- MODEL TEST DATA

Model weights, grams			
Model	Before test	After test	Weight loss
FB-2	648.3536	626.8013	21.5523
FB-3	645.1155	637.0565	8.0590
FB-4	646.4422	626.9398	19.5024

Dimensional measurements

	Length, in.		Diameter, in.		
Model	Before test	After test	Before test	After test max.	After test min.
FB-2	2.891	2.881	2.933	2.921	2.822
FB-3	2.895	2.895	2.932	2.924	2.903
FB-4	2.889	2.884	2.931	2.920	2.835

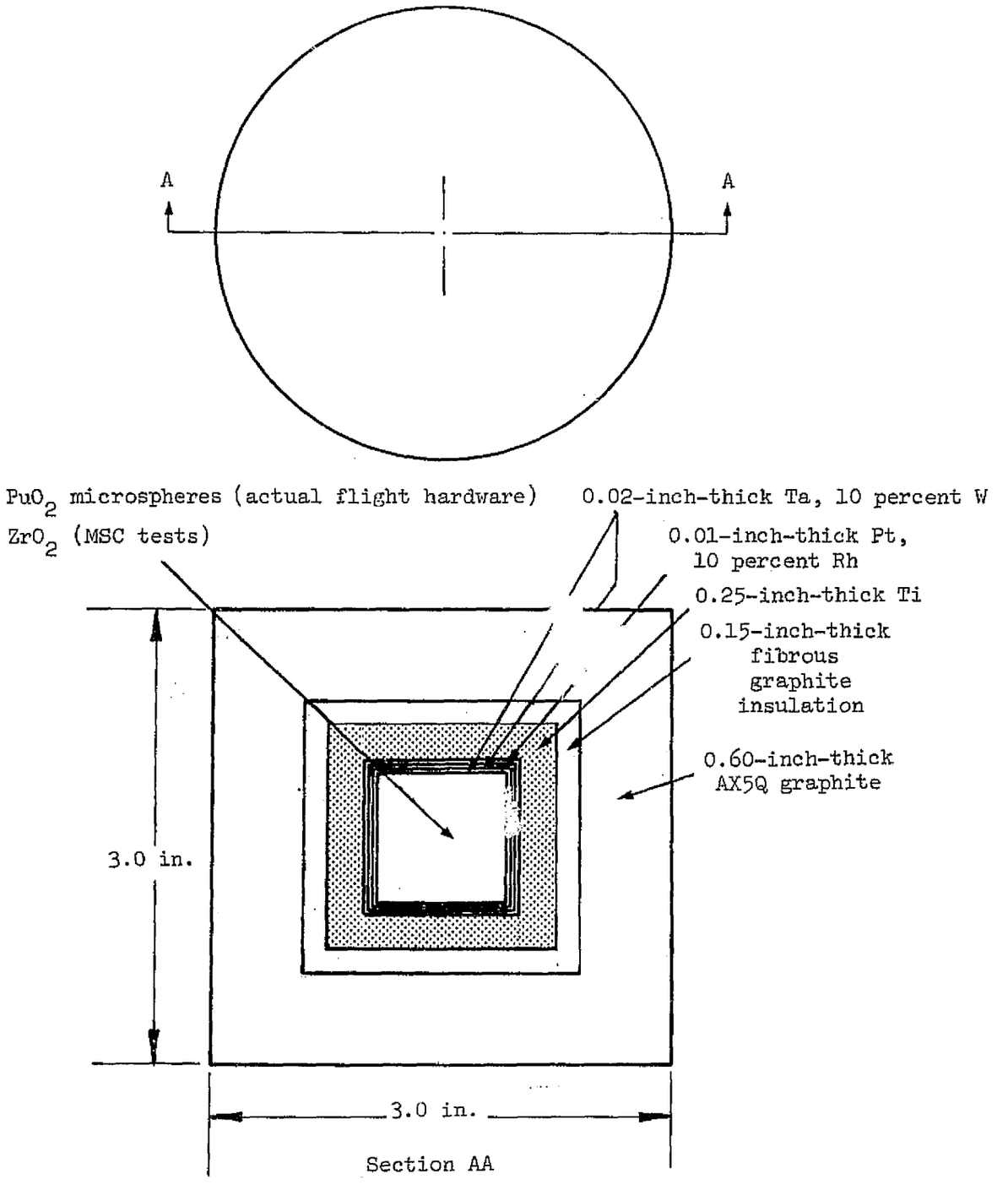

Figure 1.- Isotope heater assembly.

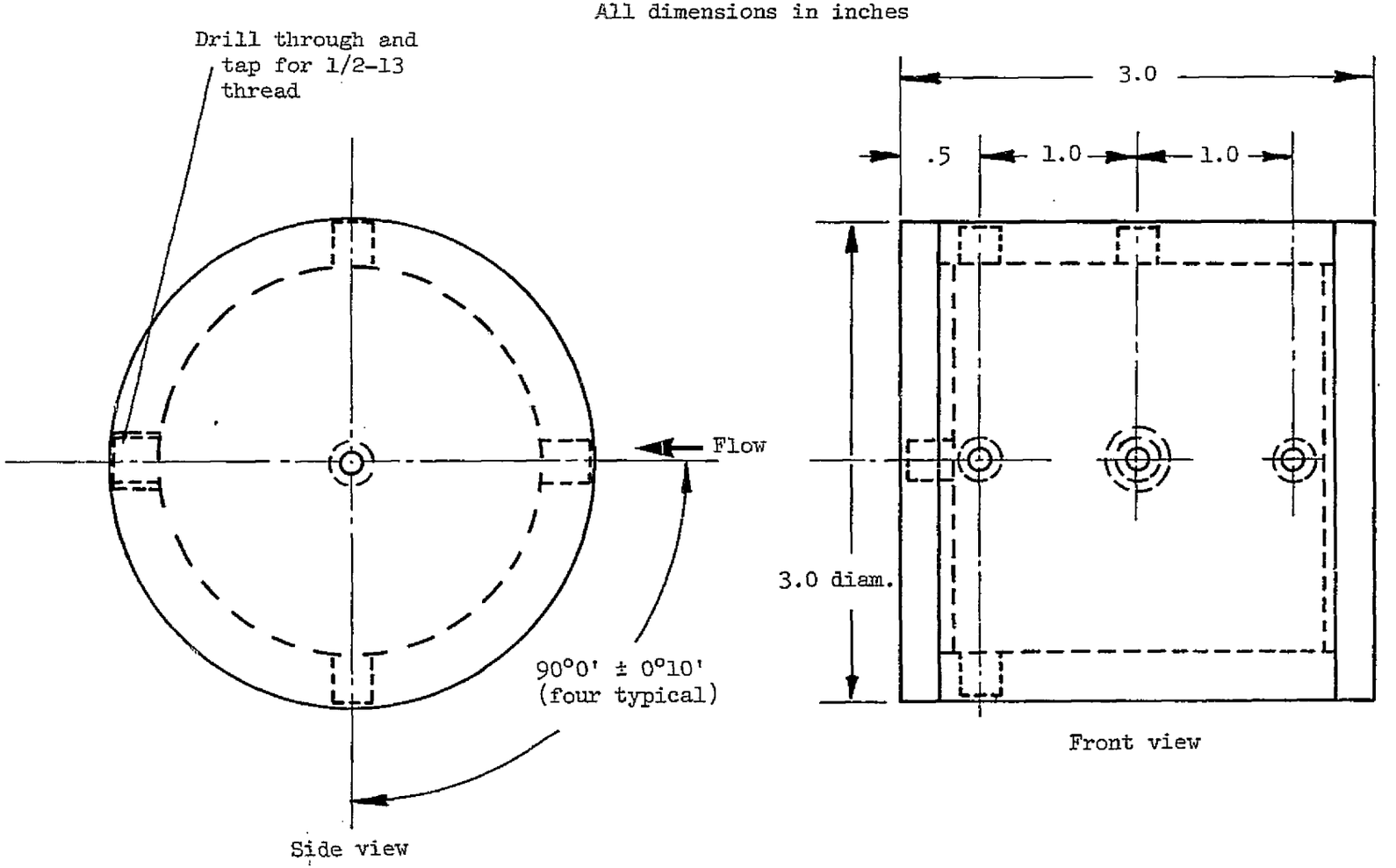

Figure 2.- Graphite heating rate calibration model.

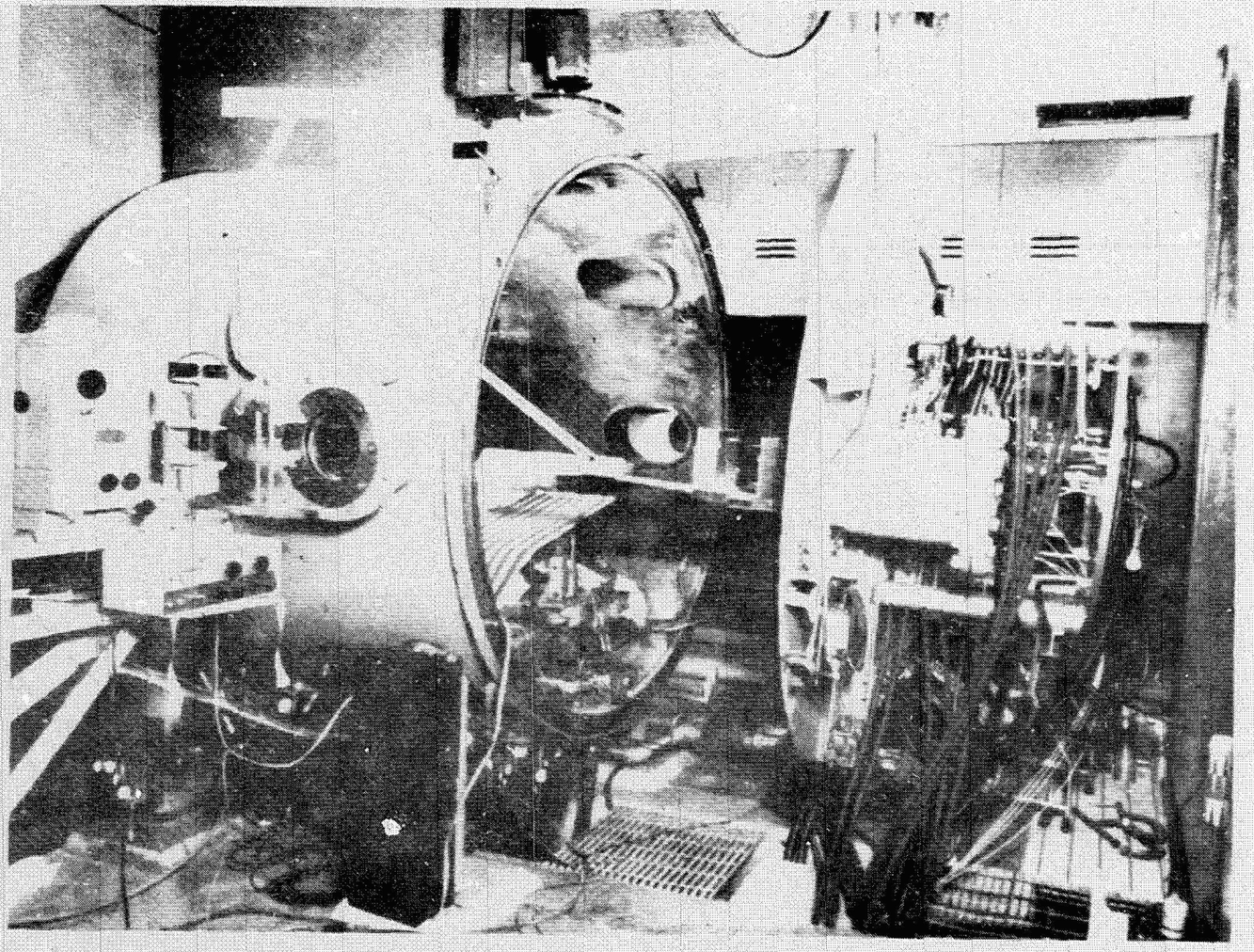

Figure 3.- The NASA MSC 1.5-megawatt arc tunnel facility.

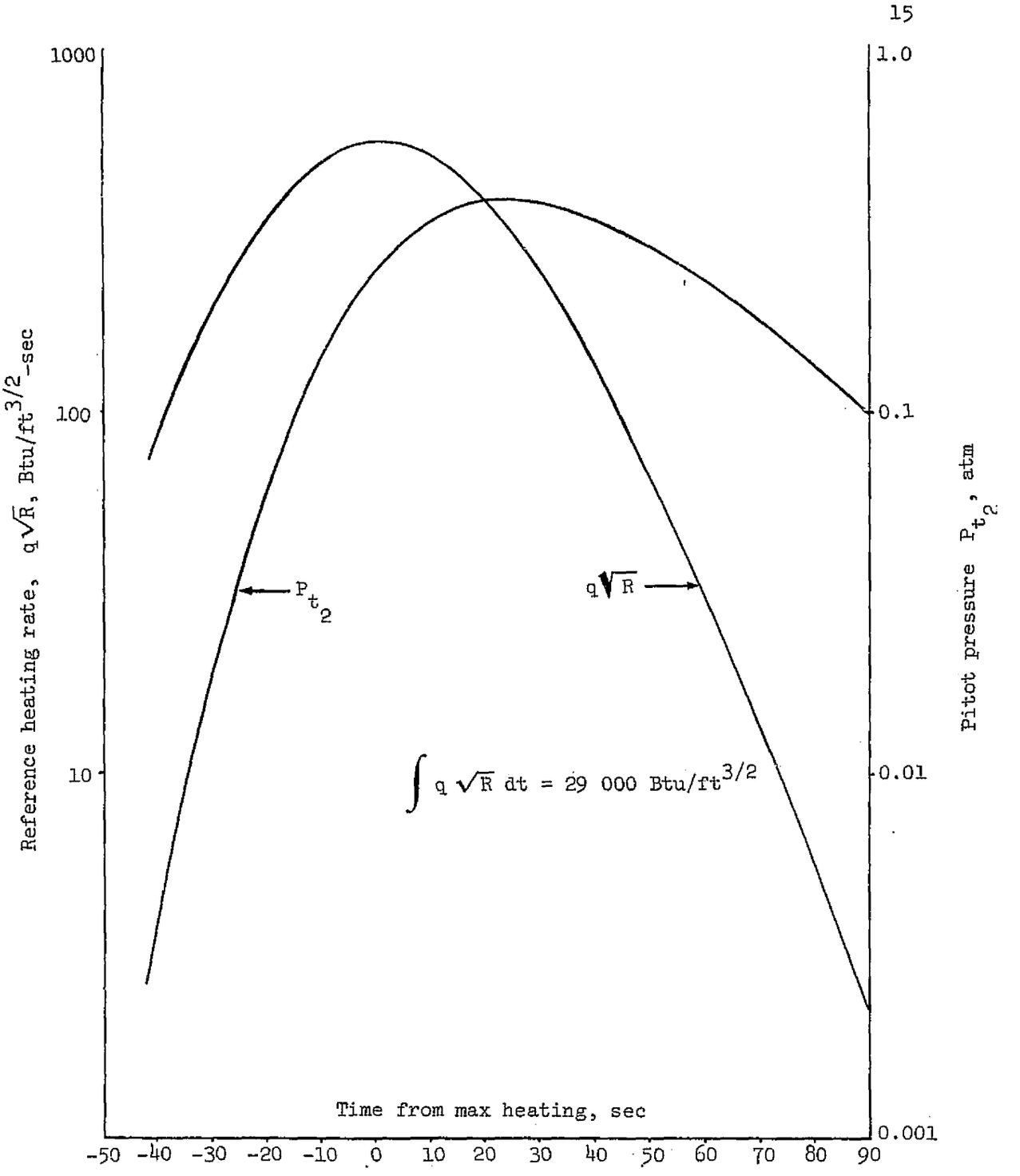

Figure 4.- Stagnation point heat transfer rate and pitot pressure on the EASEP isotope heater for a 6.25° supercircular lunar-return abort trajectory.

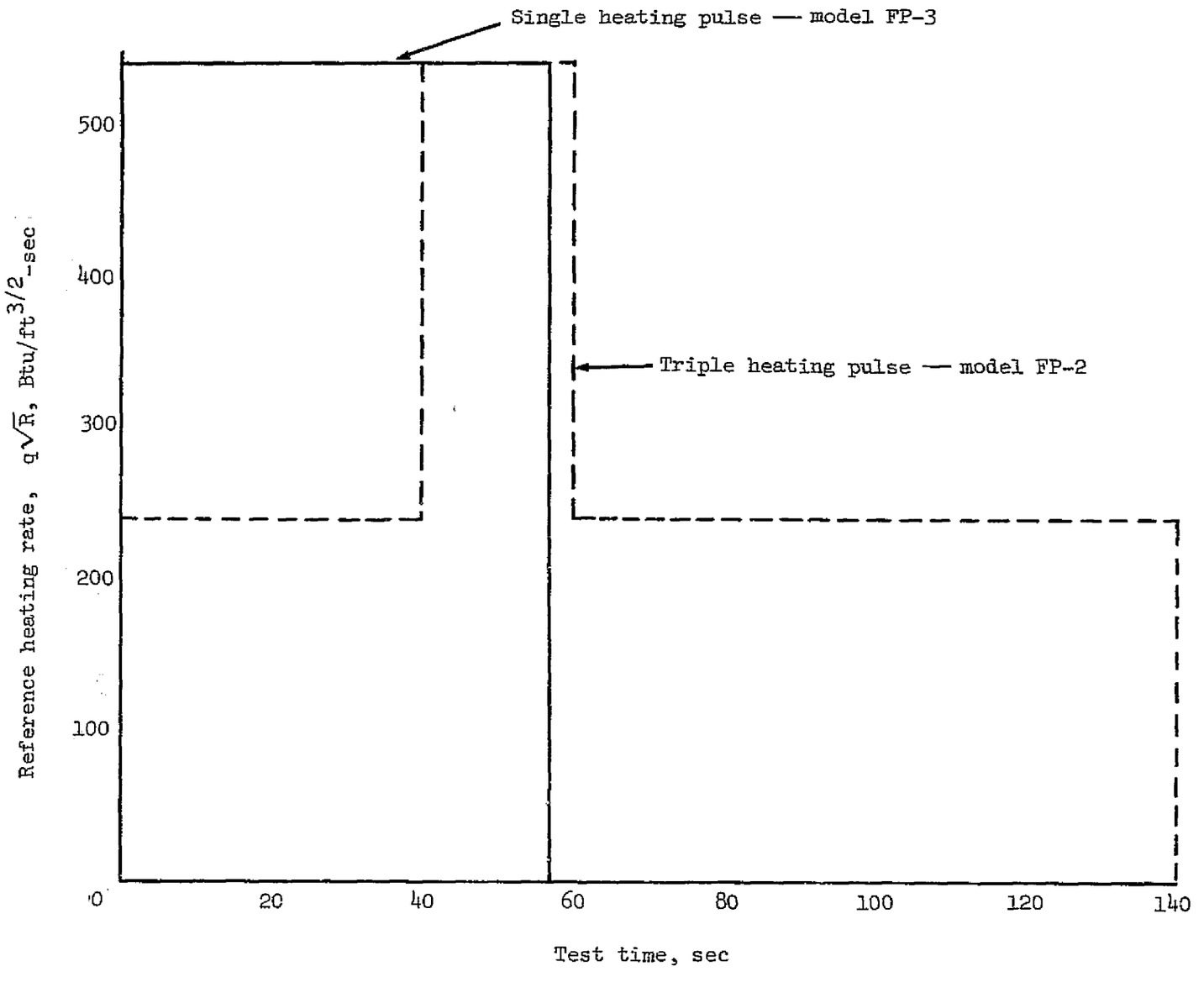

Figure 5.- Test models heating conditions.

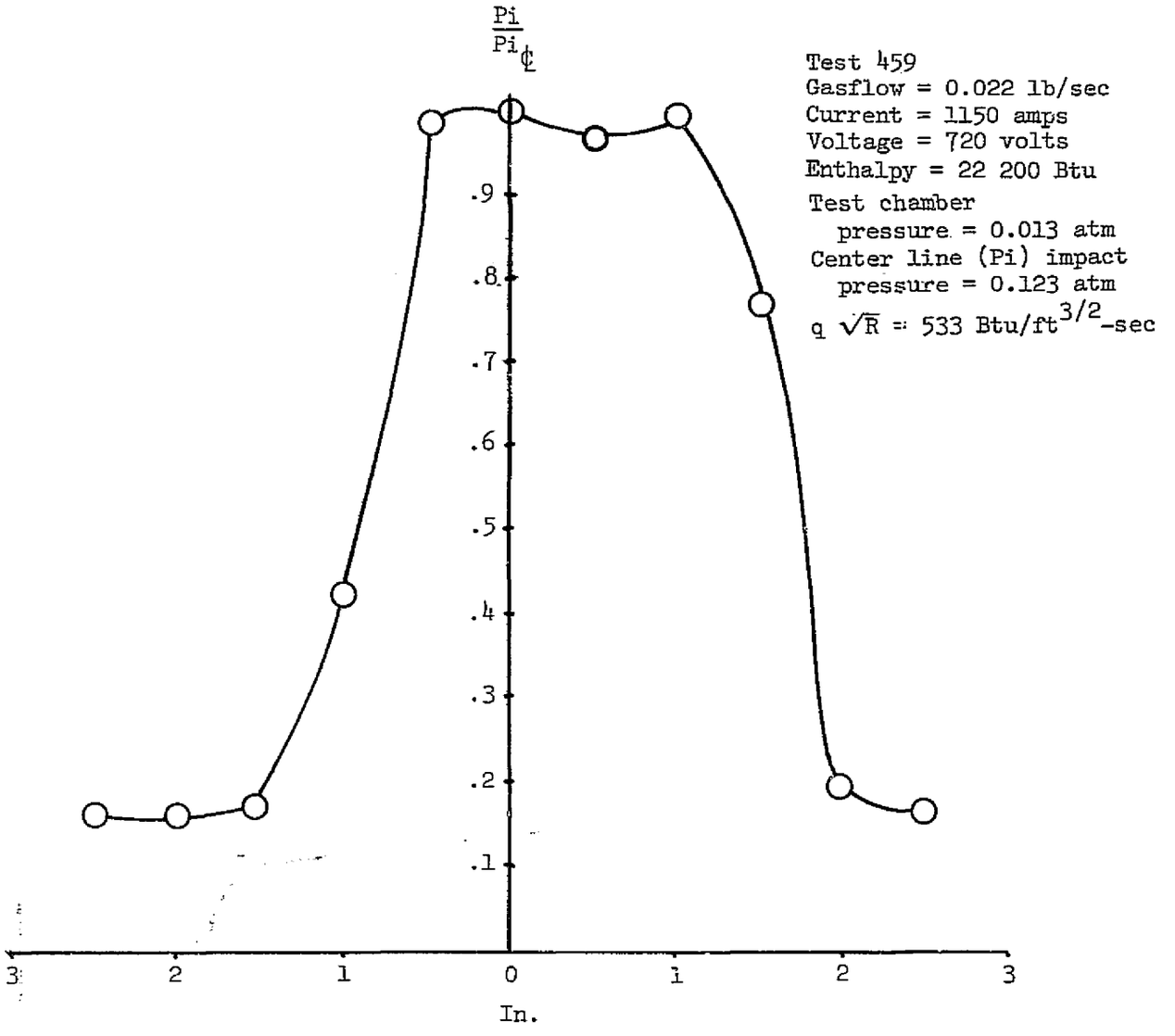

Figure 6.- Impact pressure distribution across 6.0-inch-diameter nozzle of high enthalpy arc heater at high heating rate test point.

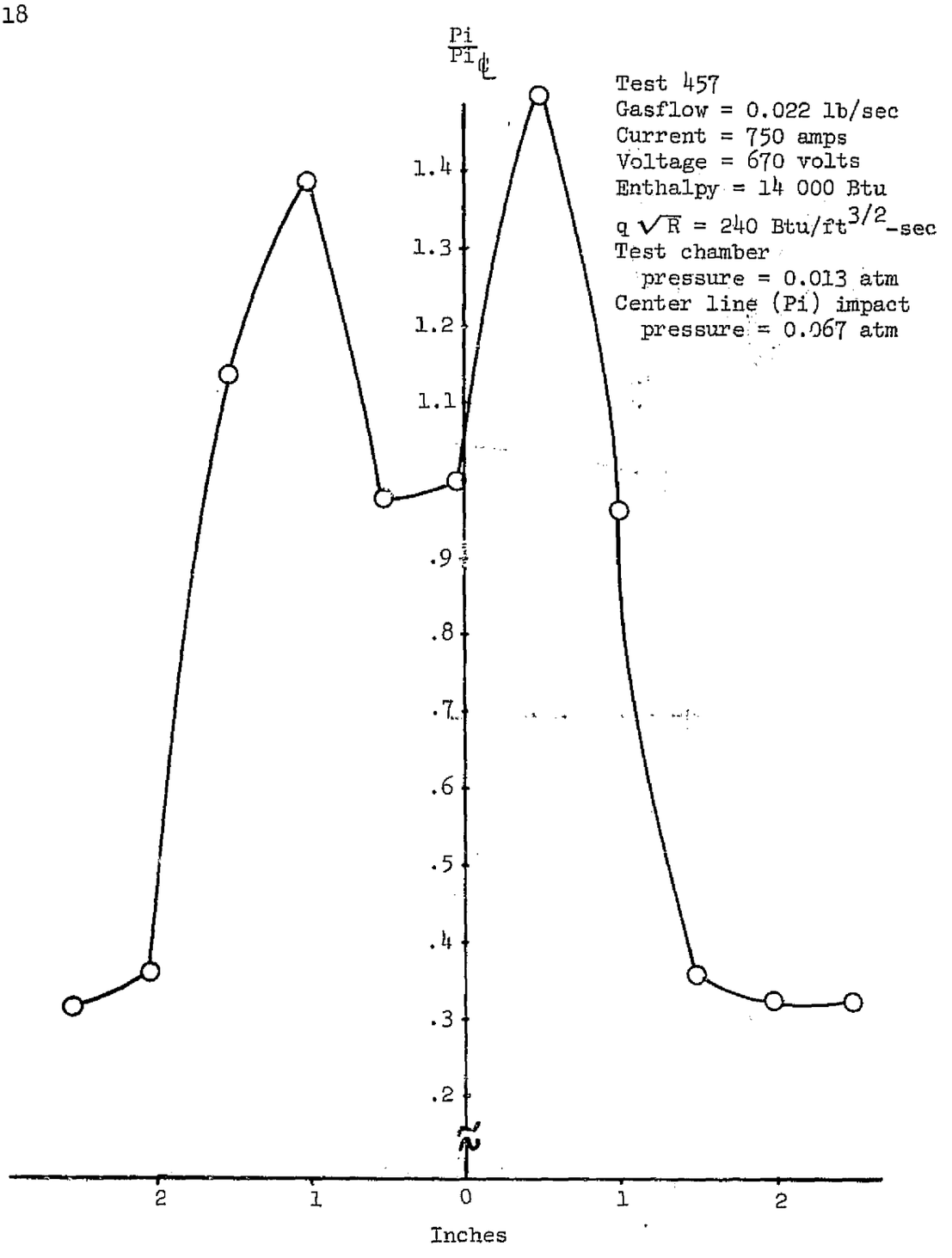

Figure 7.- Impact pressure distribution across 6.0-inch-diameter nozzle of high enthalpy arc heater at moderate heating rate test point.

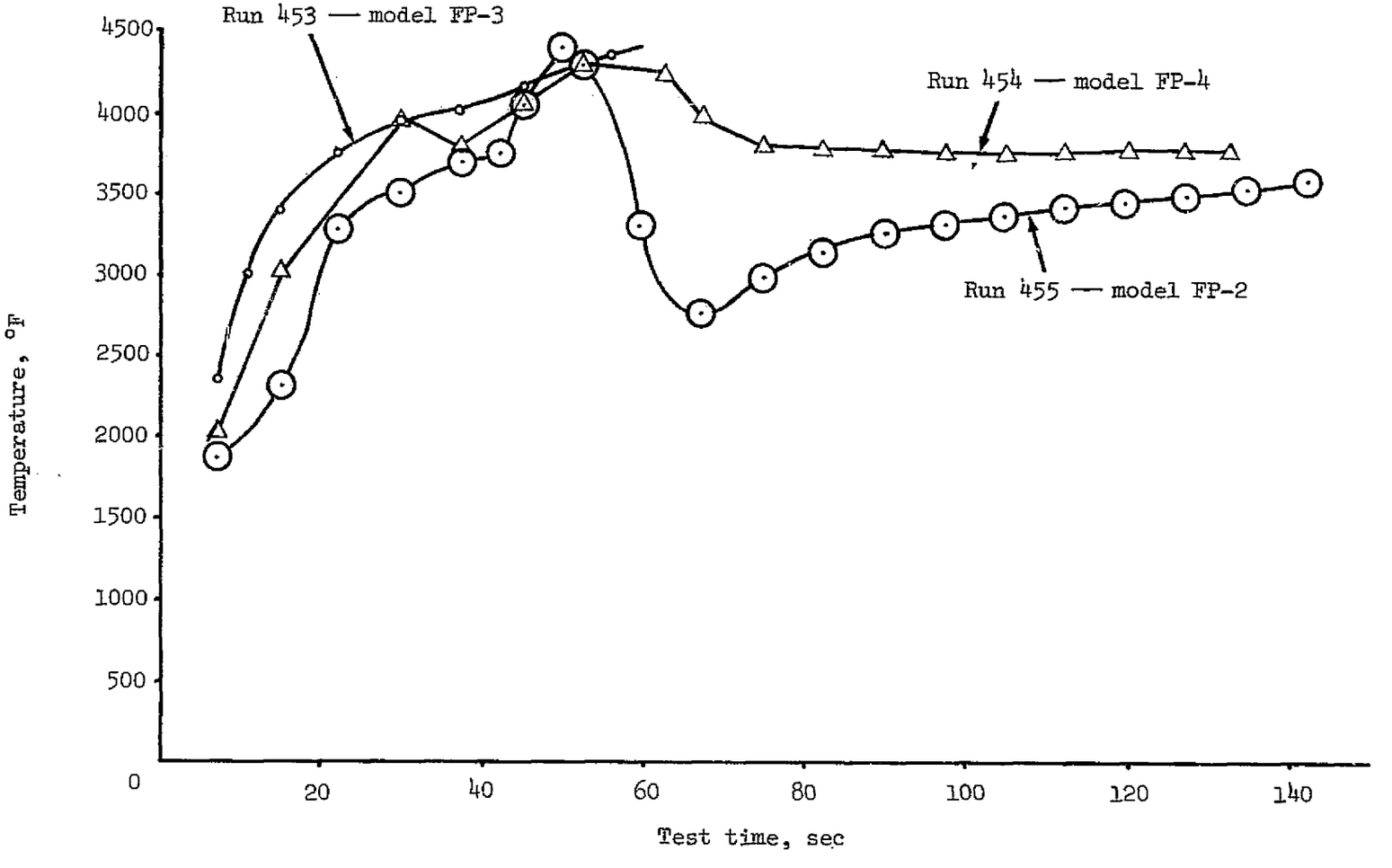

Figure 8.- Test model surface temperature response.

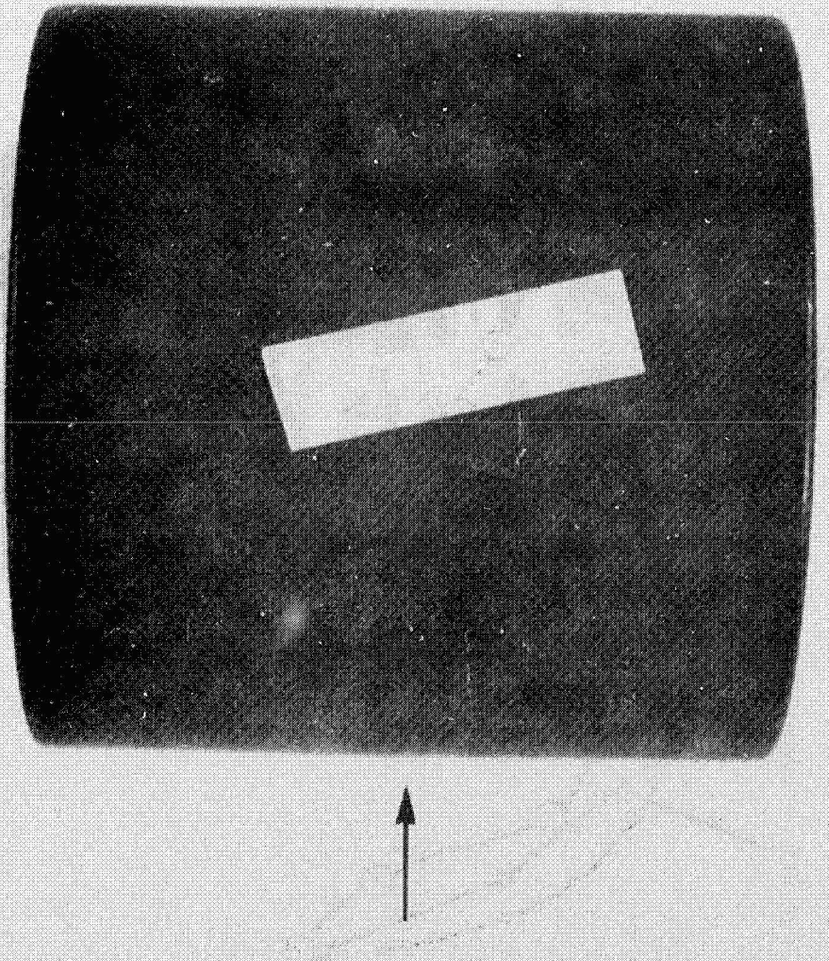

Figure 9.- Test model TP-2 before test, side view.

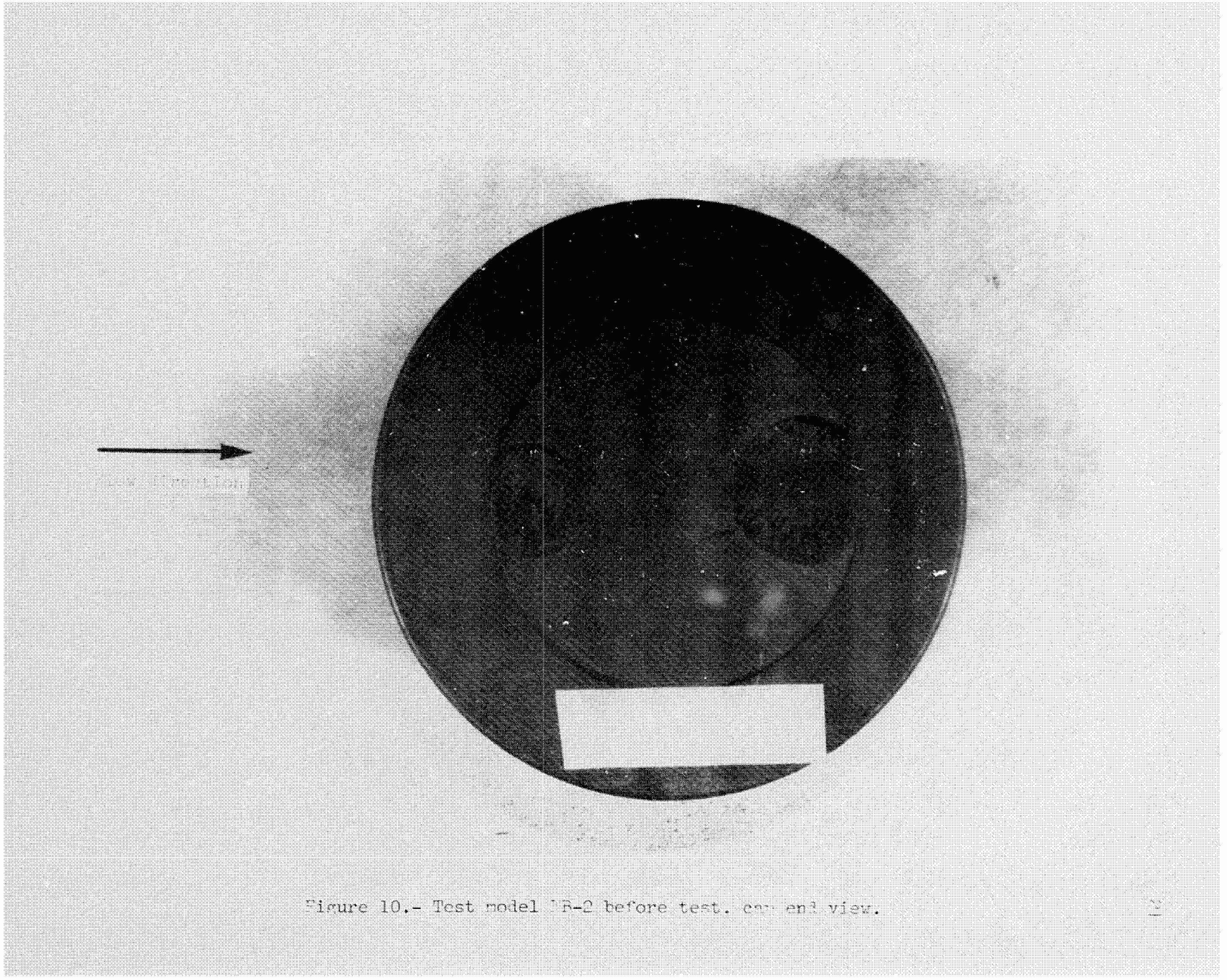

Figure 10.- Test model TB-2 before test, cavity end view.

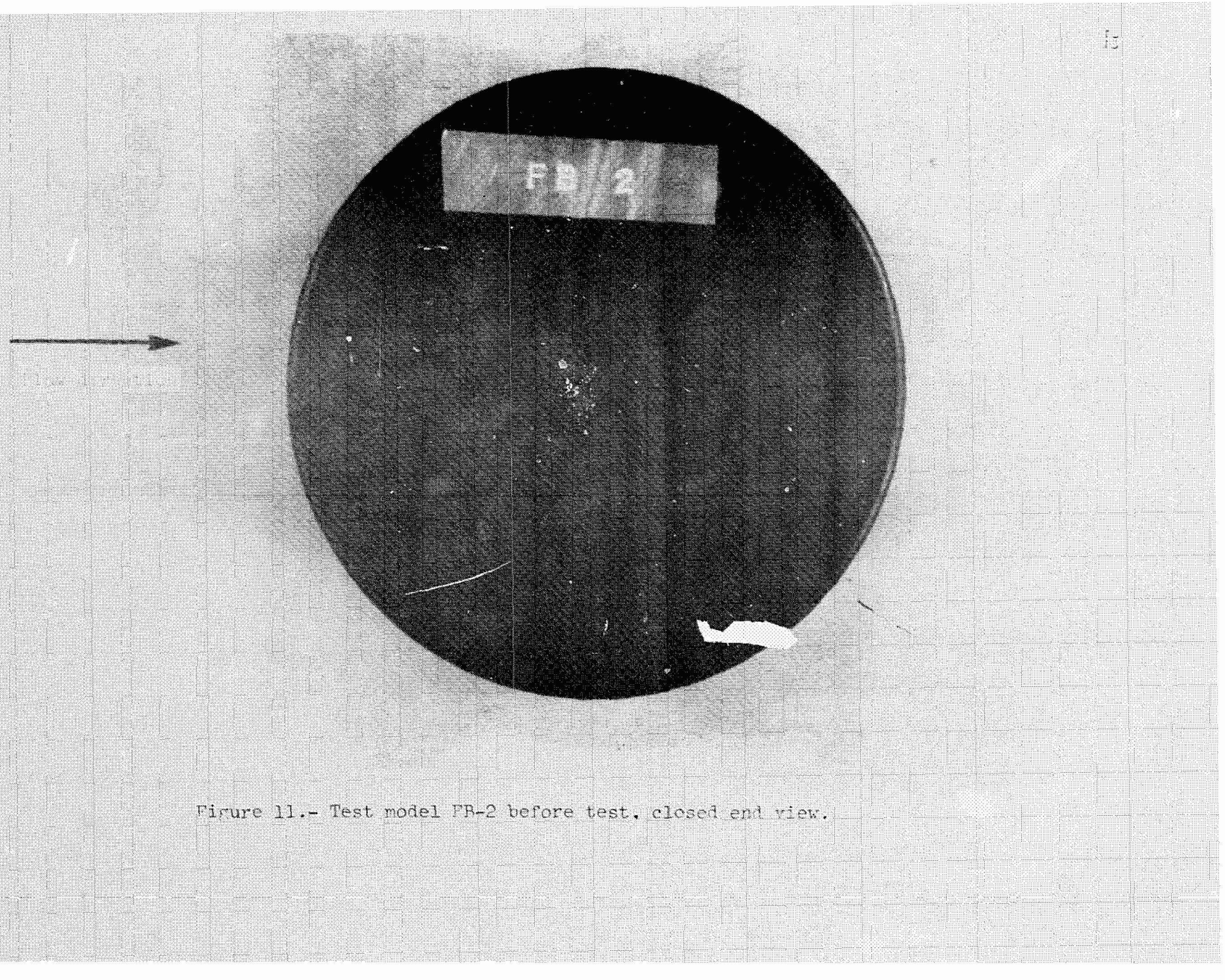

Figure 11.- Test model FB-2 before test, closed end view.

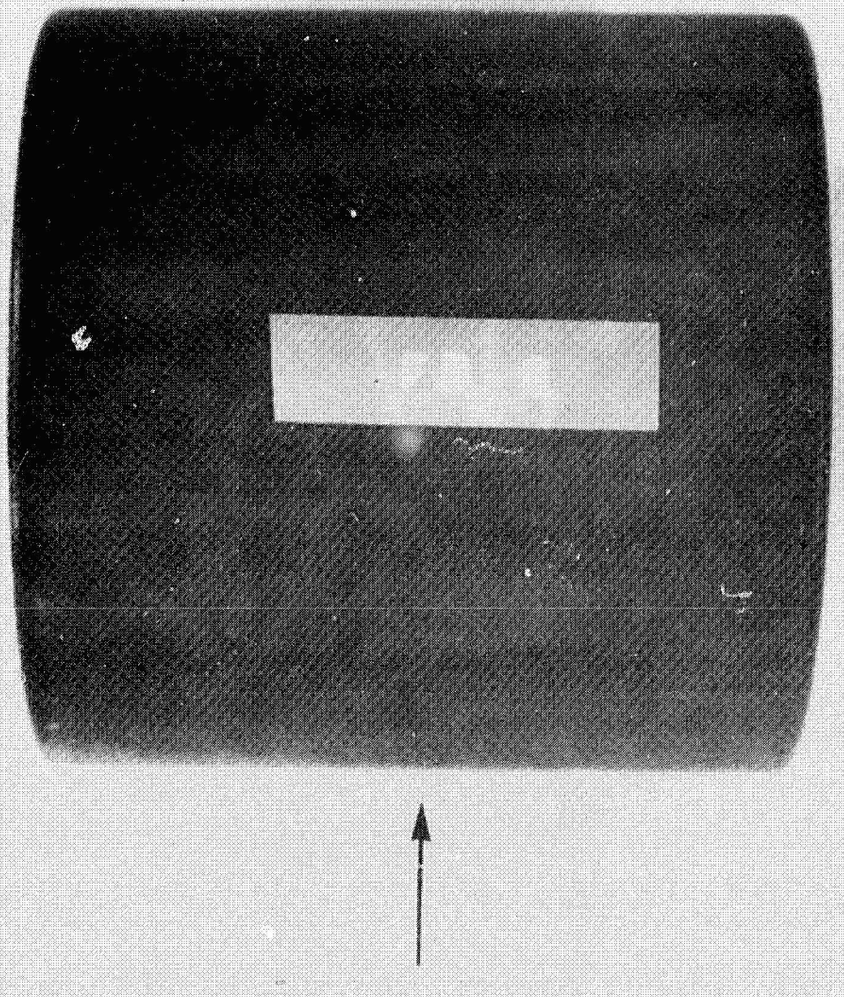

Figure 12.- Test model TB-3 before test, side view.

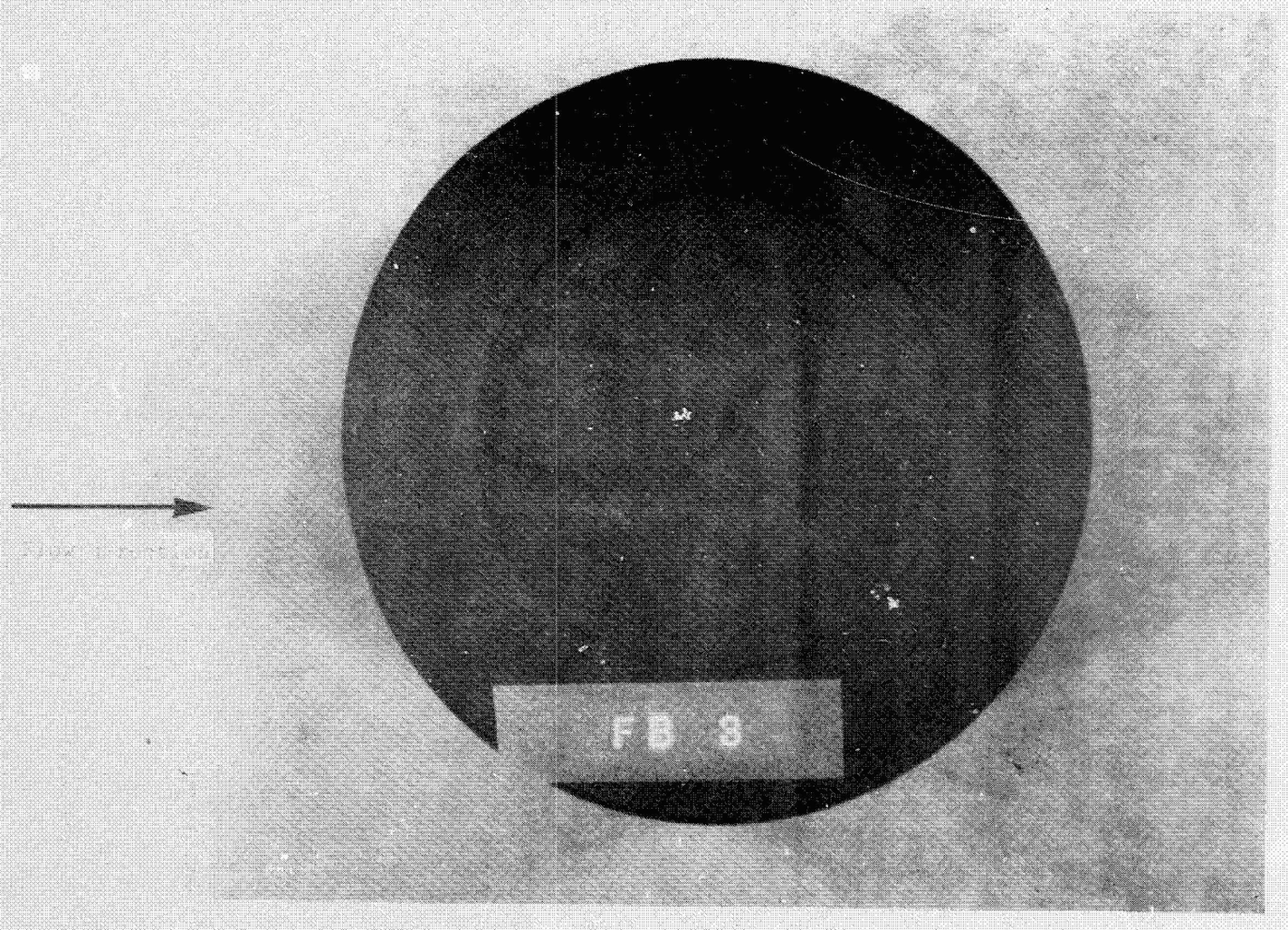

Figure 13.- Test model FB-3 before test, cap end view.

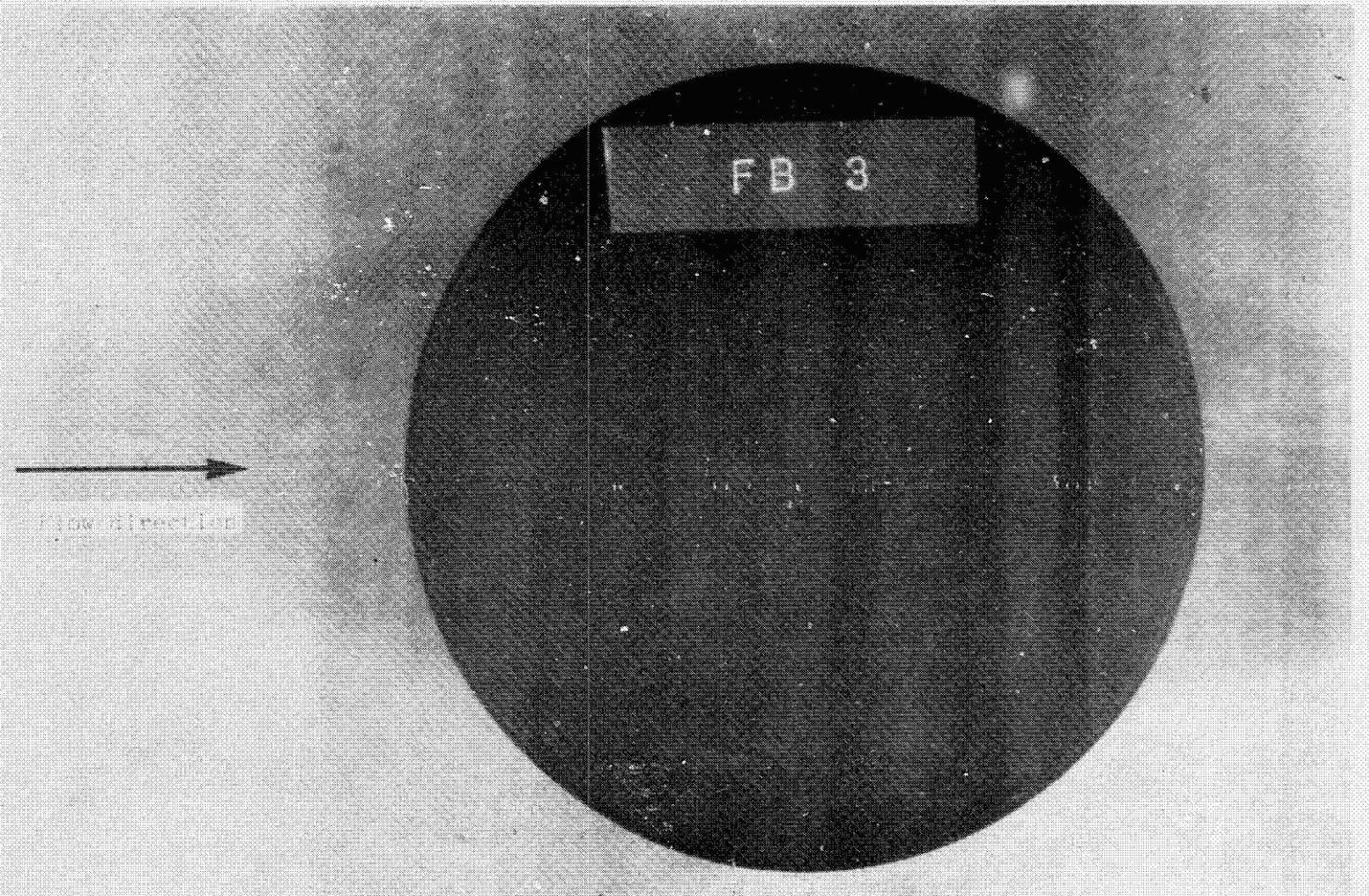

Figure 14.- Test model FB-3 before test, closed end view.

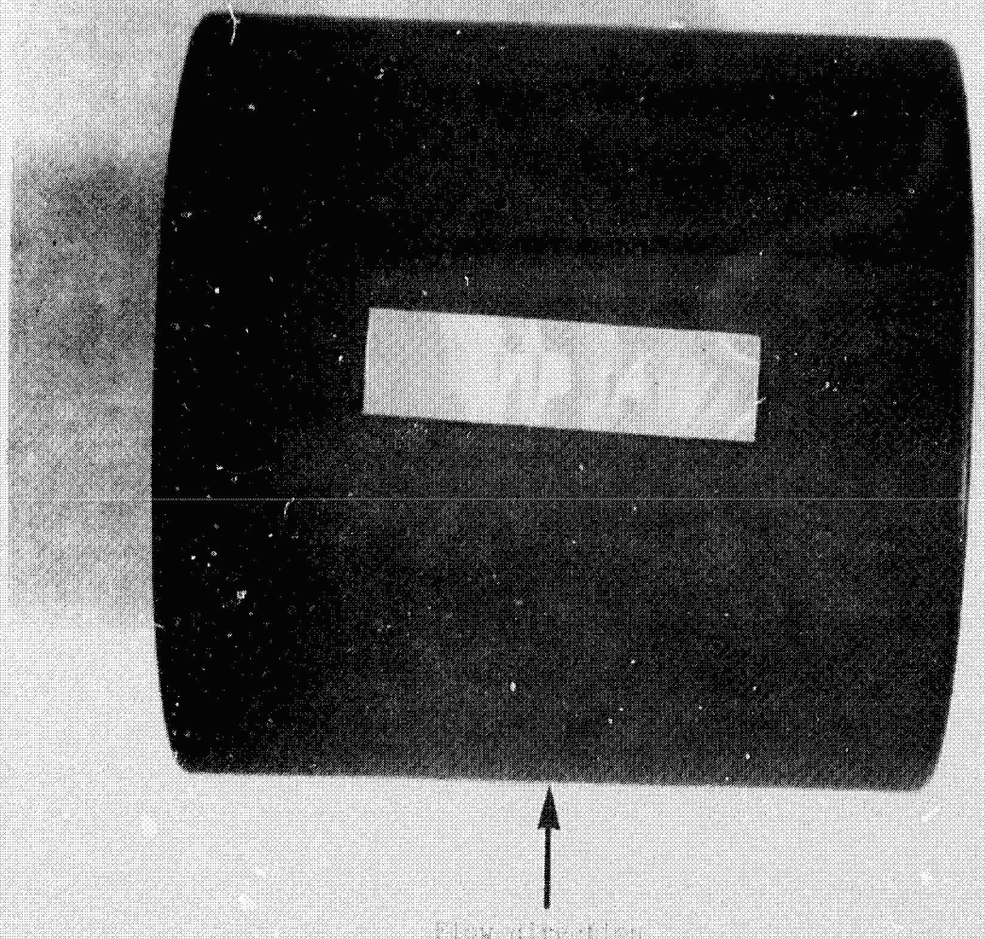

Figur 15.- Test model TR-4 before test, side view.

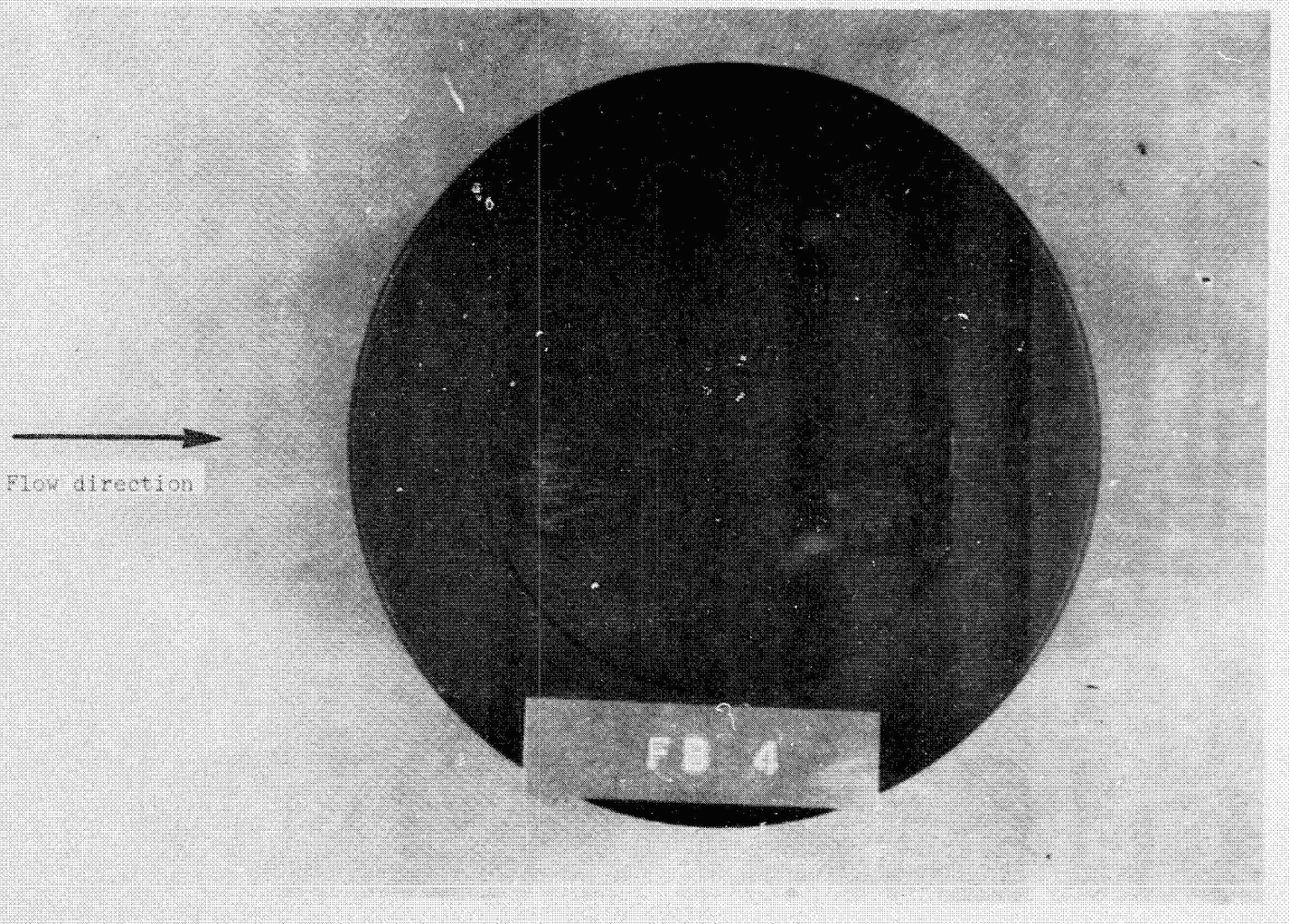

Figure 16.- Test model FB-4 before test, cap end view.

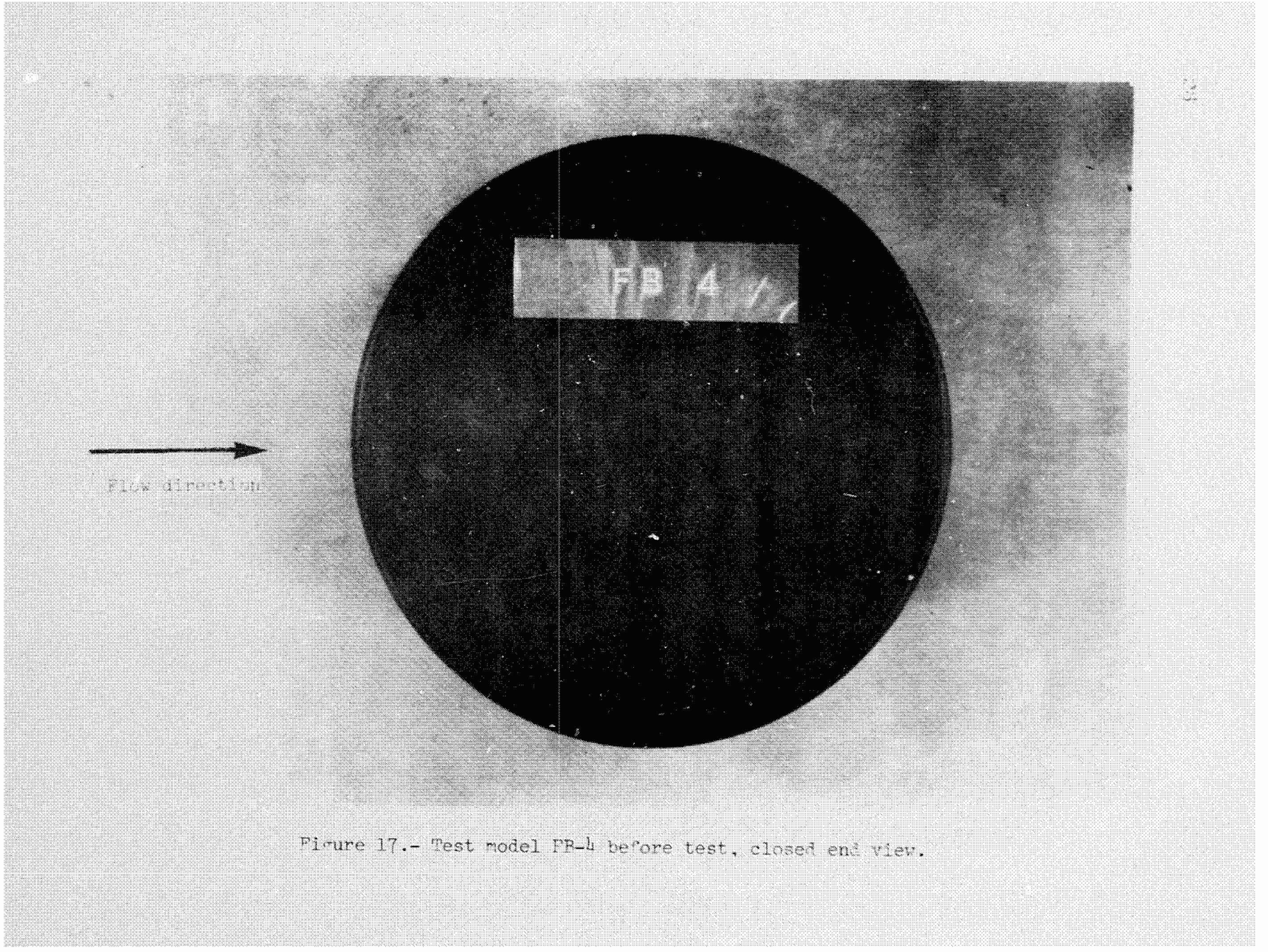

Figure 17.- Test model FB-4 before test, closed end view.

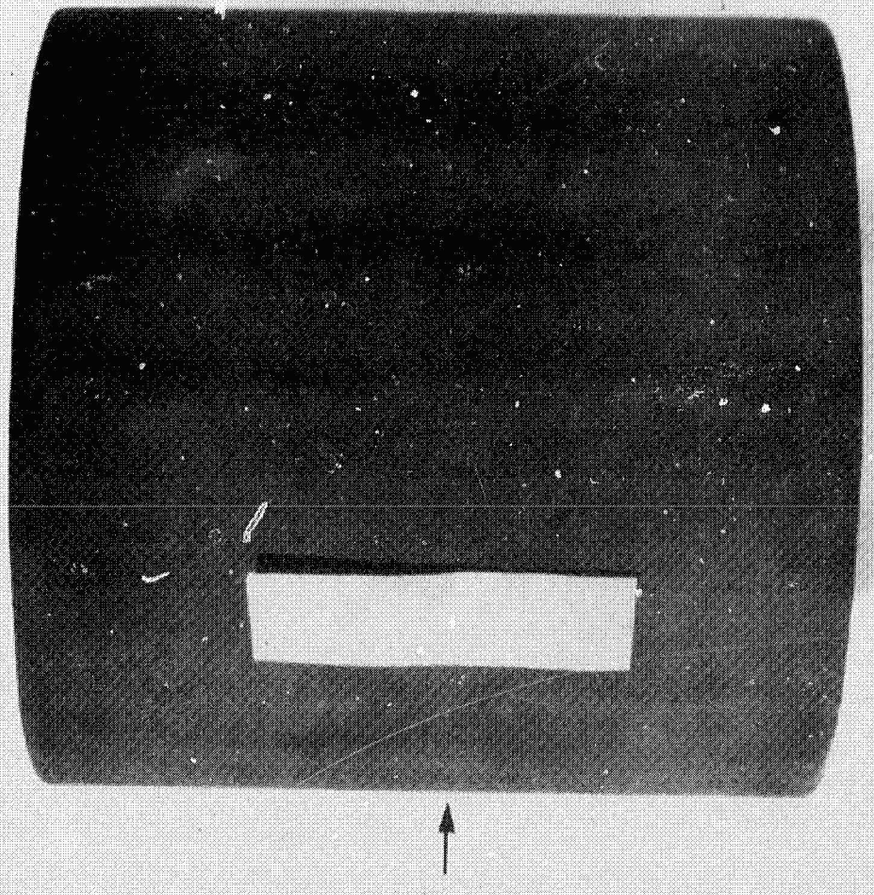

Figure 18.- Test model FP-2 after test, side view.

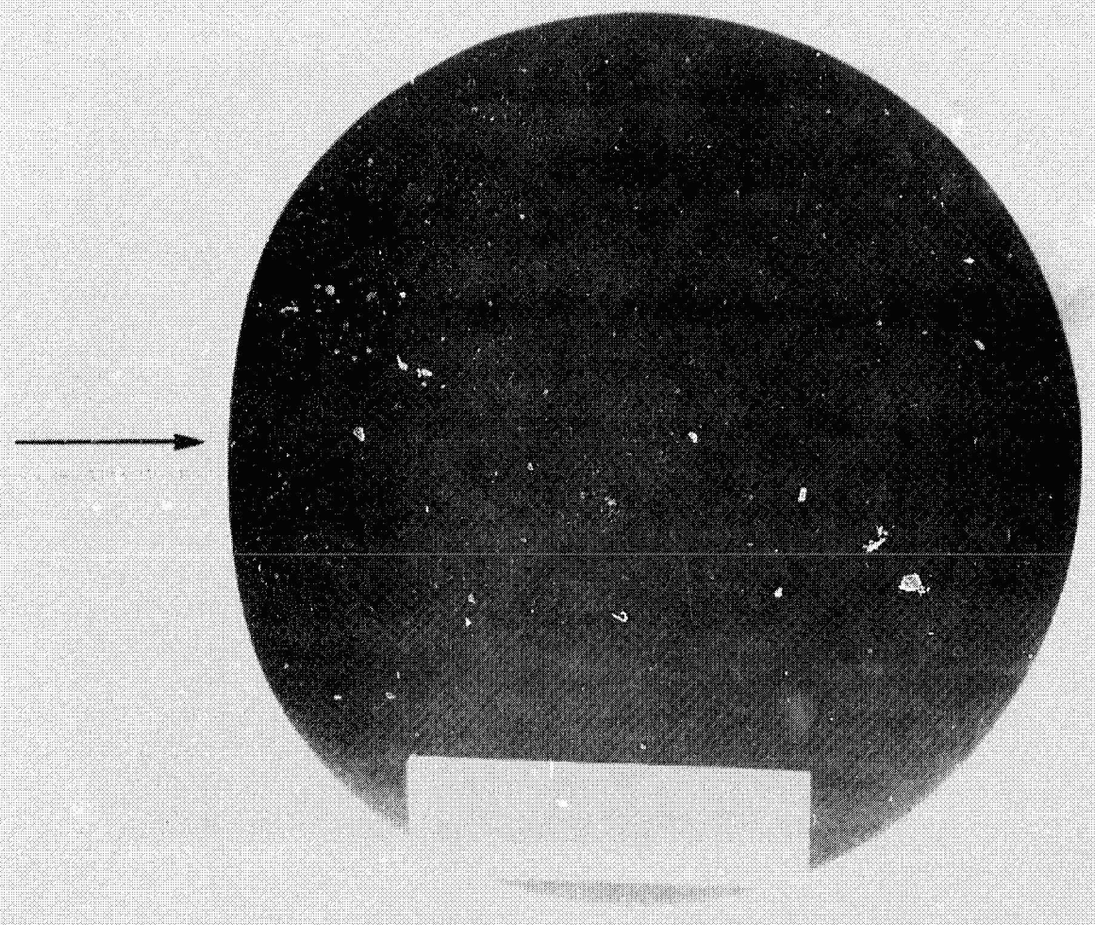

Figure 19.- Test model TT-2 after tests, aft end view.

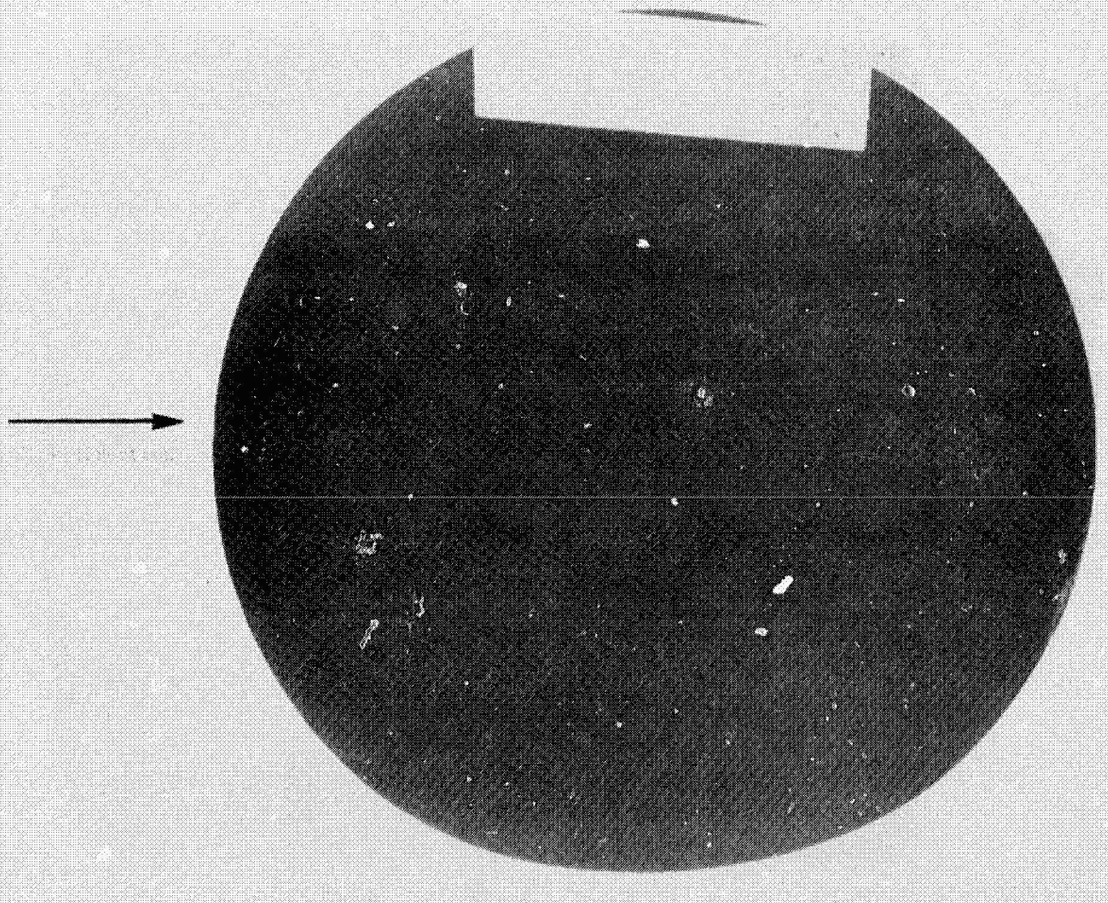

Figure 20.- Test model TB-2 after test, closed end view.

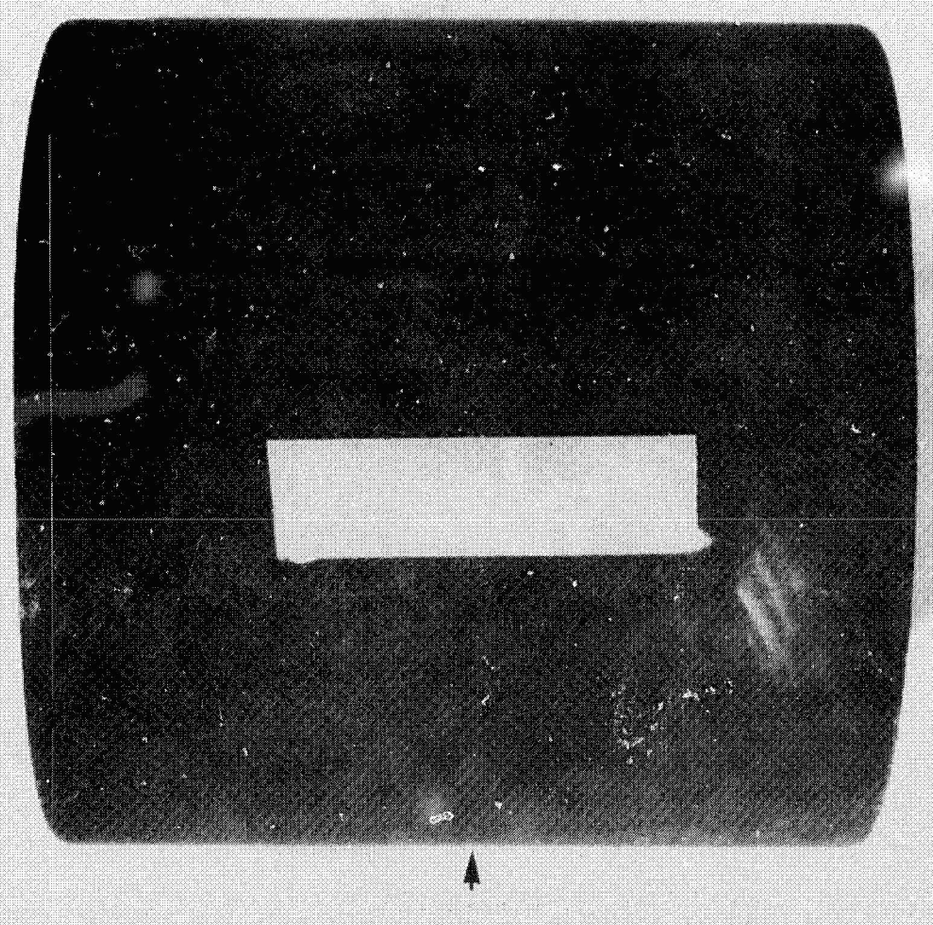

Figure 21.- Test model TB-3 after test, side view.

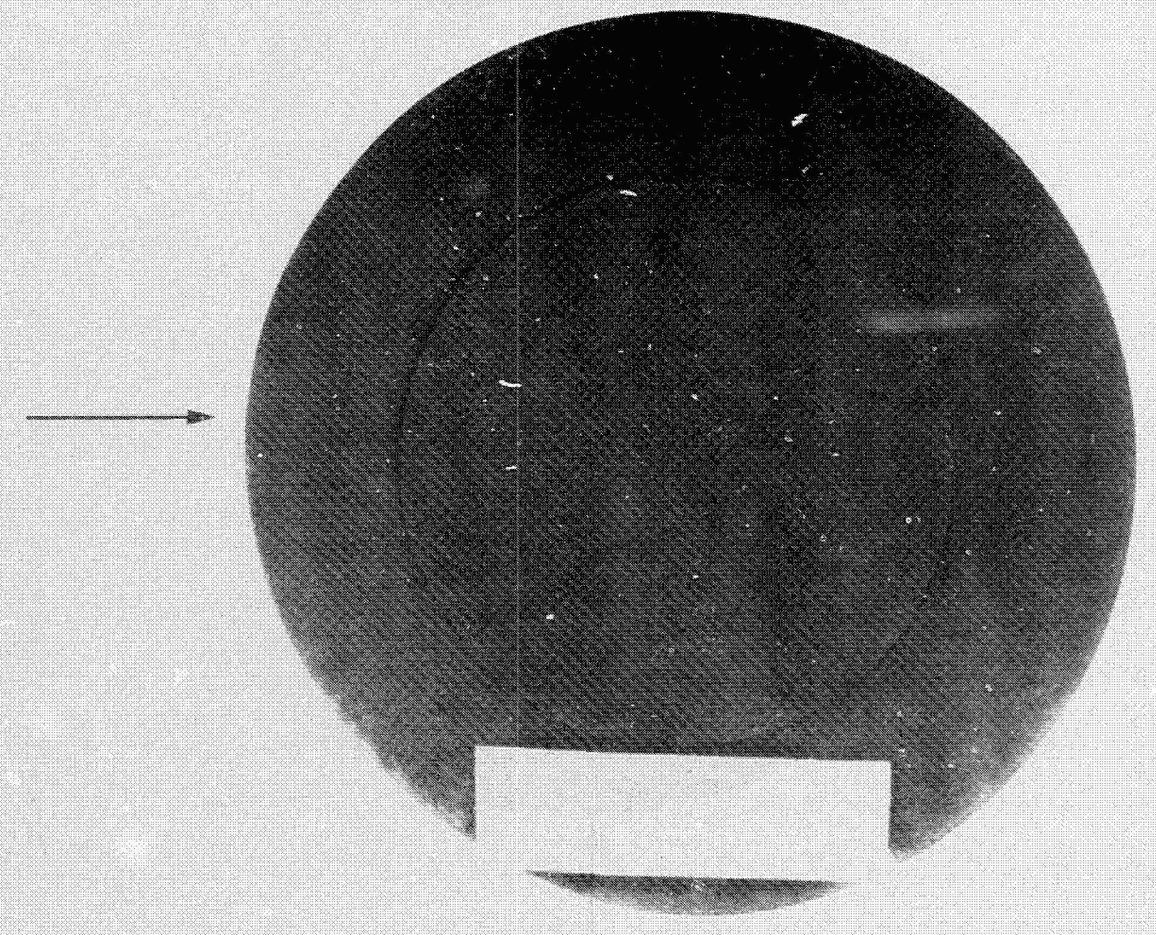

Figure 22.- Test model FB-3 after test, car end view.

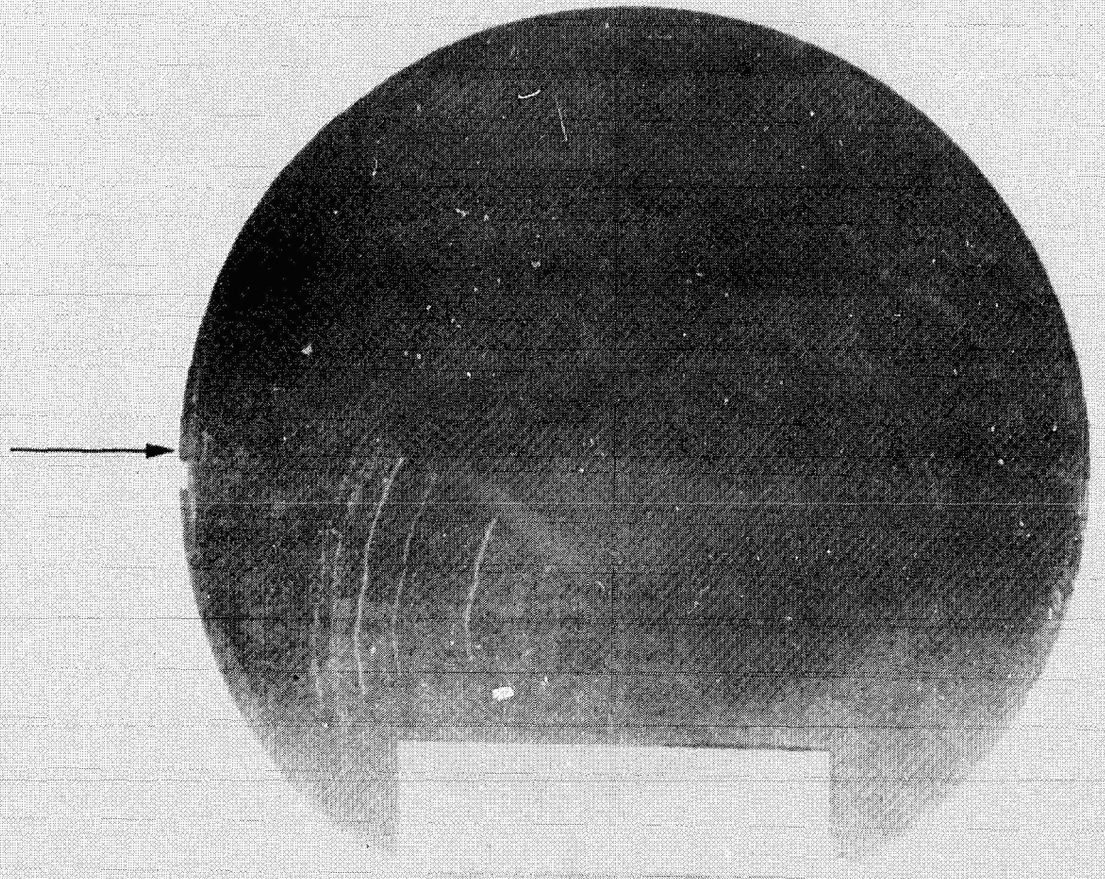

Figure 23.- Test model FR-3 after test, closed end view.

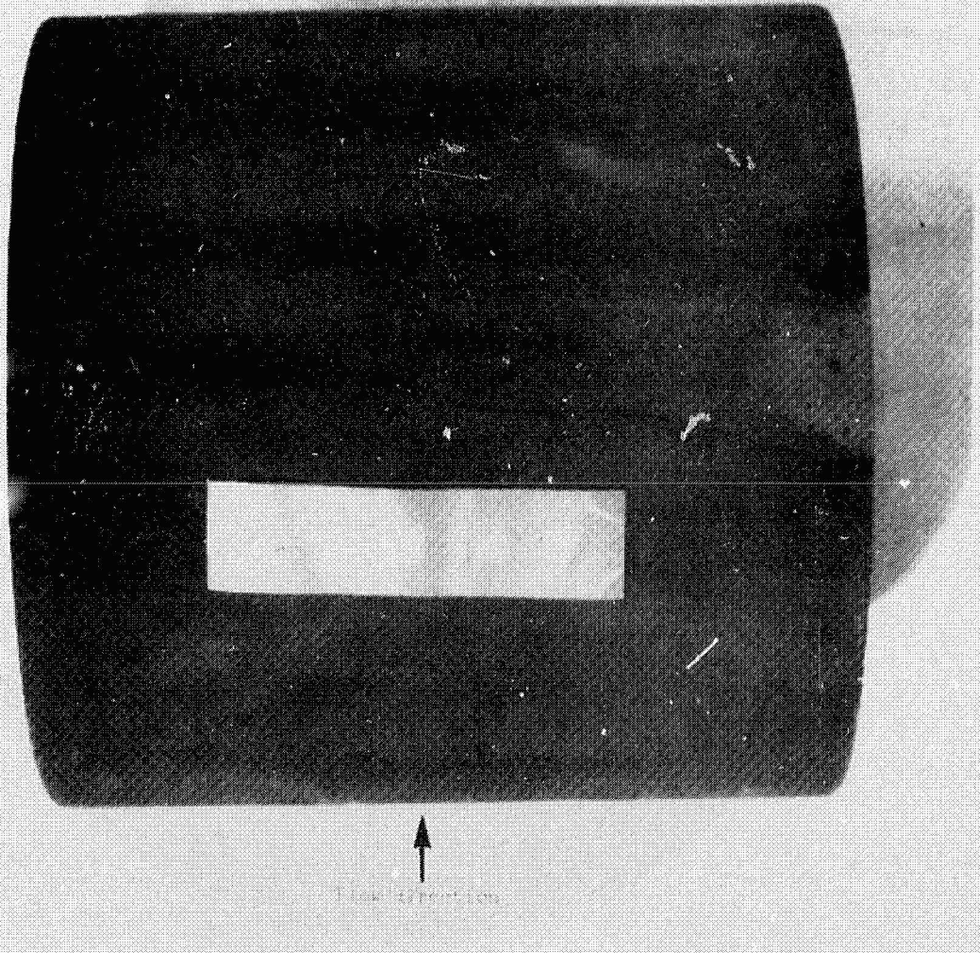

Figure 24.- Test model TF-4 after test, side view.

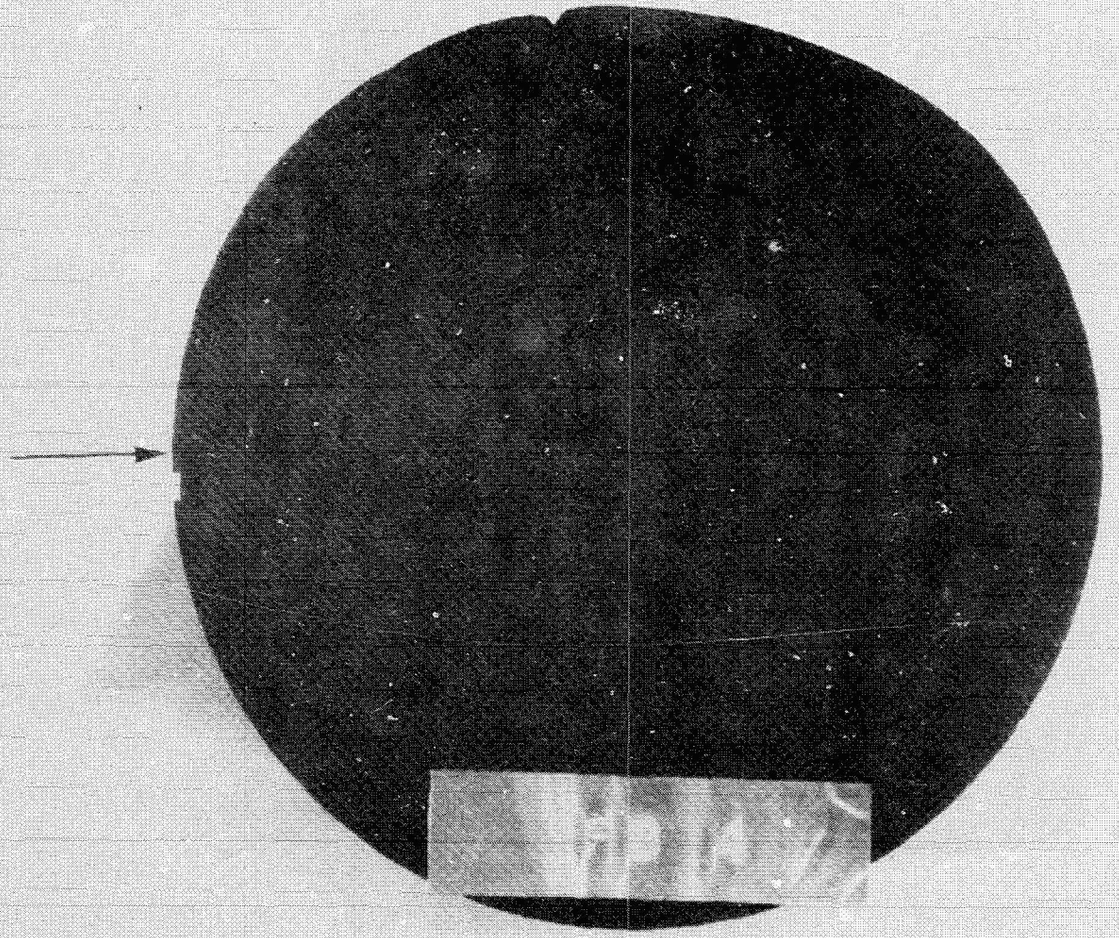

Figure 25.- Test model TB-4 after test, car end view.

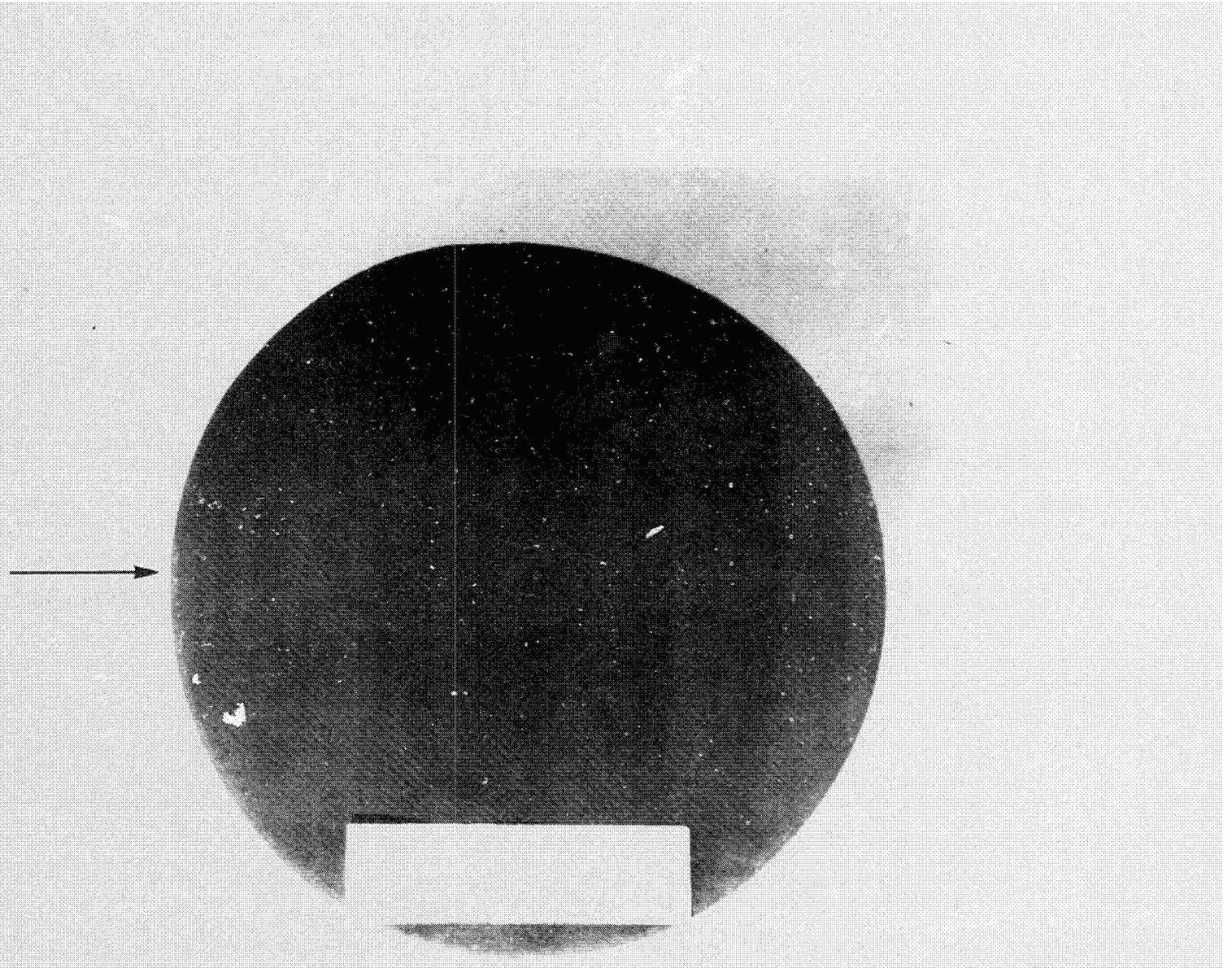

Figure 26.- Test model TB-4 after test, closed end view.